

DeepFracture: A Generative Approach for Predicting Brittle Fractures

Yuhang Huang[†] Takashi Kanai[‡]
The University of Tokyo

[†]nikoloside@gmail.com , [‡]kanait@acm.org

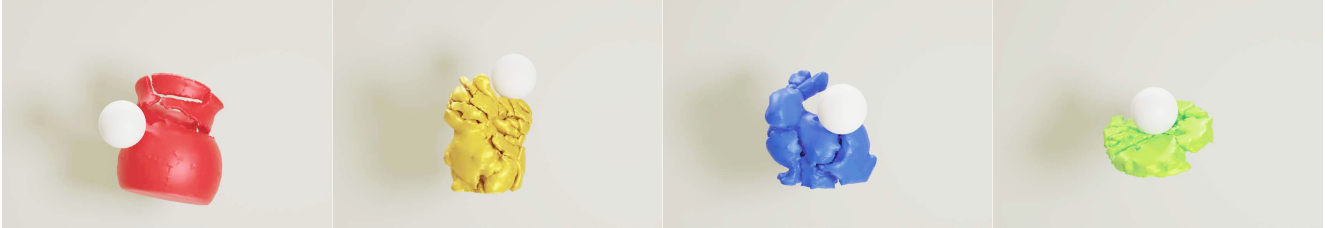


Figure 1. We introduce a novel learning-based approach for generating brittle fracture animations integrated with rigid-body simulations. This approach trains a generator per shape based on a BEM brittle fracture simulation training data. With our method, brittle fracture patterns can be rapidly predicted using impulse information. This allows for the seamless continuation of rigid-body simulations upon collision detection.

Abstract

In the realm of brittle fracture animation, generating realistic destruction animations with physics simulation techniques can be computationally expensive. Although methods using Voronoi diagrams or pre-fractured patterns work for real-time applications, they often lack realism in portraying brittle fractures. This paper introduces a novel learning-based approach for seamlessly merging realistic brittle fracture animations with rigid-body simulations. Our method utilizes BEM brittle fracture simulations to create fractured patterns and collision conditions for a given shape, which serve as training data for the learning process. To effectively integrate collision conditions and fractured shapes into a deep learning framework, we introduce the concept of latent impulse representation and geometrically-segmented signed distance function (GS-SDF). The latent impulse representation serves as input, capturing information about impact forces on the shape’s surface. Simultaneously, a GS-SDF is used as the output representation of the fractured shape. To address the challenge of optimizing multiple fractured pattern targets with a single latent code, we propose an eight-dimensional latent space based on a normal distribution code within our latent impulse representation design. This adaptation effectively transforms our neural network into a generative one. Our experimental results demonstrate that our approach can generate significantly more detailed brittle fractures compared to existing techniques, all while maintaining commendable computational efficiency during

run-time.

1. Introduction

Brittle fracture animations bring impressive effects to CG applications such as video games, movies, and VFX. Through brittle fracture simulations, objects subjected to brittle fractures dynamically form patterns and fragments based on collision forces, enriching and adding realism to the destruction representation.

Physics-based destruction simulation methods can generate intricate and realistic cracks by identifying where the initial cracks occur through stress and strain analysis and calculating the displacement of the cracks in multiple time steps frame by frame. However, current physics-based simulation methods [6, 10], including those utilized within the film industry, necessitate computationally intensive simulations.

In real-time applications like virtual reality or games, a more popular and appealing alternative involves creating a pre-fractured pattern during the modeling stage and switching from the original model to the fractured pattern upon collision. Several proposed methods [25, 33] can dynamically determine the number and size of destruction patterns or fragments in advance. However, these methods, which frequently employ Voronoi diagram segmentation for speed and reliability, face difficulties in diversifying fragment distribution or shape when confronted with arbitrary external forces. This challenge makes it hard to accurately represent

complex real-world fracture patterns.

To address the issue of weak-structure-aware pre-fractured patterns and their adaptation to arbitrary external forces, Sellán et al. [35] introduced a technique for rapidly creating pre-fractured shapes through worst-case structural analysis. This method is generally quick and suitable for real-time applications such as video games. However, while it effectively enhances the visual appeal of shapes with weak structures, it struggles to accurately simulate realistic fracture patterns in more complex shapes.

In this paper, we introduce a novel approach for generating brittle fracture patterns utilizing 3D generative networks. Our approach facilitates the seamless incorporation of brittle fracture pattern prediction into rigid-body simulation systems, exemplified by the Bullet Physics simulation engine [5]. We reconceptualize the challenge of brittle fracturing for arbitrary shapes, viewing it as a conditional generative fracture pattern prediction. This perspective seeks to link the pre-collision state with the post-collision fractured pattern observed during immediate destruction.

Our methods contain two main processes: 1) In the learning process, our framework employs the BEM brittle fracture simulation (informed by Bullet Physics simulation) [10] to generate training data reflecting collision scenarios and their resultant fracture patterns. To achieve the conditional generation of these fracture patterns, we design a customized conditional generator model and employ a novel training framework. Note that we refine a conditional generator specifically tailored to a target shape. 2) In the run-time process, we employ the Bullet Physics simulation engine as the foundation for our real-time operations. Upon collision detection of a target shape by the Bullet Physics simulation, we capture the impulse data. This data, once transformed into a *latent impulse representation*, is then processed by the designated conditional generator for the target shape to predict the fracture pattern. Subsequently, the original shape is replaced by this fractured pattern, equipped with rigid-body attributes. The simulation then continues, and the results are rendered as animations.

Specifically, our technical contributions can be categorized as follows:

- To rapidly predict fractured patterns during run-time, we employ 3D voxel-based CNNs instead of implicit function-based networks, which often utilize MLP. This choice eliminates the need for point cloud sampling during the inference phase. To enhance the speed of inference, we depart from the traditional U-Net structure generator design and introduce a more streamlined condition-to-voxel neural network specifically designed for fractured pattern generation.
- We introduce an eight-dimensional latent space, grounded on a normal distribution code, as an integral component of our latent impulse representation design. While con-

ventional conditional-GANs [24] typically combine z real noise labels and y noise class labels as generator inputs, we incorporate position-encoding using SIREN [36] into the impulse information code. Additionally, we employ an eight-dimensional noise code based on a normal distribution. Our findings suggest that this adaptation effectively transforms our neural network into a generative paradigm.

- Aiming to enhance the generator’s adaptability to unfamiliar impulse data and random normal distribution codes in run-time, we introduce a unique training patch methodology for our GANs. This approach diverges from the conventional conditional-GANs design and aligns more closely with our customized latent impulse representation.
- To integrate our generator’s predictions into the rigid-body simulation framework and achieve high-speed prediction, we design an output prediction format using geometrically-segmented signed distance functions (GS-SDF), specifically tailored for morphological segmentation. Furthermore, we establish a pipeline to convert fractured pattern data into distinct mesh structures that possess rigid-body attributes. Our assessments indicate that this pipeline demonstrates significantly higher speed when compared to existing alternatives.

To the best of our knowledge, our approach represents a pioneering effort in addressing the challenge of fracture pattern generation. While fracture restoration, assembly, and repair predominantly focus on shape reconstruction based on a single precise input leading to a single specific output, our task emphasizes producing one of several possible outputs from a given condition. This positions our task within the generative domain of deep learning.

2. Related Work

In this section, we will explore related works in fracture animation, focusing on both physics-based and real-time aware methods. Furthermore, we will provide an overview of recent research concerning learning-based fracture tasks and techniques.

2.1. Physics-based simulation

Physics-based fracture simulation methods can create complex and realistic cracks by calculating the displacement of the cracks frame by frame. However, it can sometimes take hours to generate a single frame of fracture animation. Consequently, their usage is typically limited to applications with substantial computational resources, including movie VFX, artistic control, and engineering analyses.

Terzopoulos and Fleischer were pioneers in proposing a fracture model within the realm of CG [38]. Subsequently, various methods emerged, including those based on spring-mass systems [22, 27], FEM [3, 28, 29], BEM [9, 10], XFEM [4], XDEM [13, 14], Graph-based FEM [21], and MPM [6]. Initially developed in the field of engineering, these methods

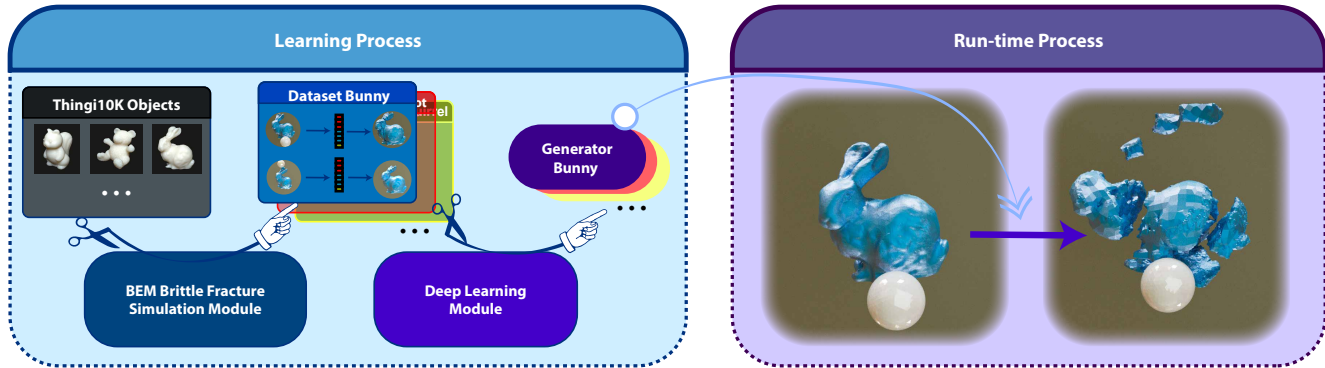


Figure 2. Our method’s framework proposes two processes: a learning process and a run-time process. With the BEM brittle fracture simulation module and deep learning module, we can generate a specific condition-to-voxel generator tailored to the target $t \in \mathcal{T}$ and the target shape S^{origin_t} . The run-time process integrates the generator with the rigid-body simulation module to help rigid-body simulation seamlessly continue to generate fracture scenes without brittle fracture simulation.

have found applications in the domain of CG. Notably, the fracture simulation using BEM [9, 10] only uses the data structure of the surface, not the volumetric structure of the 3D object, to generate the fractured meshes. This allows for generating more efficient and flexible fracture surfaces and more easily integrating with rigid-body simulation systems than other physics-based methods. However, most actual simulations still require enormous computational time, spanning several hours, for linear system calculations and surface remeshing.

Huang et al. [12] proposed a data-driven method incorporating regression forests into the BEM-based fracture simulation. This approach circumvents the need for solving linear systems and creates a versatile database capable of predicting situations and models beyond those it has learned. However, it should be noted that this method still carries a significant computational cost, making it unsuitable for real-time applications.

2.2. Real-time Aware Animation

Real-time aware methods typically focus on two key aspects: 1) Calculating geometrically similar segmentation shapes for physics-based simulations on fractured objects, and 2) describing the relationship between external force loads applied to the fractured object and the resulting fractured pieces.

Geometry-based methods are generally fast and easily applicable to pre-fracture algorithms in real-time applications like video games. Among geometric-based methods for fracture animation, Voronoi diagram-based techniques [2, 26, 32] serve as a rapid alternative for determining fracture shapes instead of relying on physics-based approaches. Various methods have been proposed to address the challenge of diversifying the distribution and shape of fractured pieces when applying arbitrary external forces. Usually, these meth-

ods predefine both the fracture pattern and the quantity of fractured pieces [11, 20, 25, 37]. Müller et al. proposed a fast geometric pre-fracture method [25], which has been implemented in the NVIDIA® PhysX™ physics engine [31]. A data-driven method was introduced that utilizes RBF networks to adapt external forces to a 3D Voronoi diagram-based segmentation and predict the extent of fracture [33]. While Voronoi diagram-based segmentation is a fast and reliable method, it struggles to represent concave shapes, making it challenging to represent complex real-world fracture shapes.

To address the challenge of generating weak-structure-aware pre-fractured patterns and adapting them to arbitrary external forces, Sellán et al. introduced a technique that rapidly constructs pre-fractured shapes through worst-case structural analysis [35]. This method can handle multiple external force inputs by projecting the calculated impact onto a pre-calculated fracture mode’s linear space in real-time. However, the generation of these pre-fractured patterns relies on worst-case structural analysis, which lacks brittle fracture characteristics as it does not consider crack initiation or propagation details.

2.3. 3D Representations and Related Fracture Tasks in Deep Learning

Recently, voxel-based 3D representation, implicit function-based 3D representation, and their associated generative neural networks have demonstrated substantial progress in deep learning. The initial 3D generative networks, grounded in voxel-based representation [40], were introduced by exploring a probabilistic latent space of object shapes through 3D generative-adversarial modeling. An improved version of the voxel-based CNN methods [8] has been proposed for multitasking within generative networks for 3D model

generation.

In contrast, other advancements in 3D shape representation have been made through the learning of continuous signed distance functions, embodied in an MLP named DeepSDF [30]. Significant research has been developed, including NeRF [23] and subsequent work on 3D representation and implicit function-based generative networks. These approaches avoid the challenge of memory limitation when learning voxel-based 3D shapes and have been shown to be capable of describing 3D details. Despite their promise, implicit function-based techniques tend to have longer inference times than CNN models.

One recent development in 3D representation in deep learning is a discussion of the encoding of 3D position and activation function [36]. This work not only improved the details of 3D reconstruction in MLP networks, but also introduced an intelligent idea for encoding 3D coordinate values.

Implicit function-based 3D representation techniques have been refined for fracture repair [16–18]. These techniques can reconstruct 3D broken shapes from two pieces, which can be easily encoded as three implicit functions. Multi-part or fractured shapes assembling is another work on fractured shapes in deep learning. Sellán et al. [34] presents a database of geometric segmentation with several point cloud-based methods, all generated by [35], which focuses on weak-structure-aware shapes and assembling. Geometric segmentation, a novel concept introduced in [34], differs from multi-part and other instance segmentation tasks because it does not assume semantic information. Instead, it only considers the boundary region, which depends on geometric details.

Our task of generating fracture patterns is related to, but different from, these two tasks. Therefore, we need to develop our own dataset, adapted to our task and generated by simulation.

3. Overview

Our method creates a scenario where objects collide strongly through rigid-body simulation engines like Bullet Physics [5]. Instead of using computationally expensive brittle fracture simulations, we replace them with a deep learning process that predicts fracture patterns for arbitrary 3D shapes. This makes generating complex, brittle fracture animations possible within a reasonable computational time.

When a collision occurs at run-time, the predicted fracture pattern is immediately applied to the damaged object. Subsequently, based on the predicted pattern information, the 3D fragment shape is reconstructed. New velocities and masses are assigned to each fragment after the destruction, based on the original velocity and mass before destruction. The rigid-body simulation then continues with the updated configuration. To predict the fracture pattern, we abstract the collision information at the moment of destruction and en-

code it into a deep learning-friendly dataset, pairing the input data with the output data, which are the fractured fragments.

Figure 2 illustrates the process of our method. Our approach consists of two processes: learning and run-time. In learning, brittle fracture simulations are performed to create a training dataset, and adversarial generative networks are trained to produce the generator used in run-time. In run-time, the same rigid-body engine used in learning is employed, and the generator created in learning is utilized to predict the fracture shape.

For our method, a training dataset and a generator corresponding to the target shape are created for each shape. This means that for a new shape, a new simulation needs to be conducted through the learning process, and the generator used in run-time is trained based on the newly collected data.

4. Learning Process

In the learning process shown in Figure 3, we first adopt a series of breakable targets $\mathcal{T} = \{t_1, t_2 \dots, t_{N_{\text{target}}}\}$ from the Thingi10k dataset [41], where N_{target} is the number of breakable targets. For each target $t \in \mathcal{T}$, we define the original shape $\mathcal{S}_t^{\text{origin}}$ as the target shape. In the brittle fracture simulation module, we use the boundary element method (BEM) [10] to generate the fracture shape as training data for a single target shape $\mathcal{S}^{\text{origin}}$. Using the created training data, we train a deep learning model to produce a set of generators $\mathcal{G} = \{G_t \mid t \in \mathcal{T}\}$ for use at run-time.

4.1. Brittle Fracture Physics: Prerequisites in Our Method

Brittle fracture is a complex physical phenomenon observed in nature. Various engineering techniques simulate and predict crack initiation and propagation. To understand our proposed animation framework’s connection to extant brittle fracture physics methods, we outline the prerequisites below:

- To simplify and ensure compatibility with learning and runtime processes, we assume all fracture events occur instantaneously. Thus, primary object fragments cannot fracture further. Alternatively, we capture the BEM brittle fracture simulation over 1-100 frames and choose the final fractured shapes (with refracturing) for our dataset.
- To further simplify and abstract the fracturing process during data generation, we use a collision scenario between a breakable object and an unbreakable sphere target.
- When a collision has multiple contact points, we use the largest impulse value on the surface as our prediction input.
- We set gravity to 0 in the dataset creation scene. Our framework does not consider the weight of the breakable object to be a contributing factor to its fracturing.
- We restrict the variables impacting the fracture process of breakable objects to the collision’s position and the direction and magnitude of the impulse on its surface.

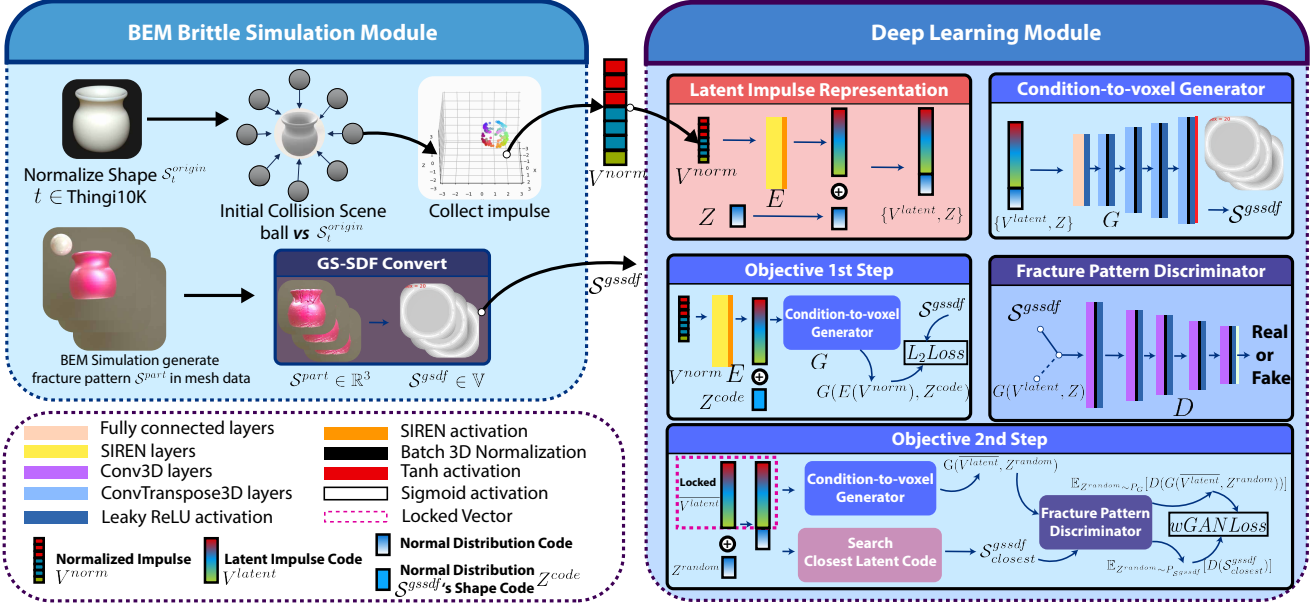


Figure 3. Our learning process consists of two modules: We first design a scene to describe the collision and set some requirements to show our method’s connection with brittle fracture physics. Consequently, we generate data by sampling the collisions between the ball and target shape S^{origin} . We then collect the segmentation S^{part} transformed into the GS-SDF S^{gsdf} . We pass the generated data through the BEM Brittle Simulation Module and Deep Learning Module. The Deep Learning Module learns the two-step objectives and finally provides a condition-to-voxel generator G for the run-time process.

- Additionally, our trained generator is tailored to a specific set of physical material parameters. As such, any alteration in material parameters is necessary to re-running both the simulation and learning modules.

4.2. Creating Learning Data

The potential data format for the deep learning training input data during collisions includes impulse information, external forces acting on the mesh surface, and kinetic energy before and after the collision. In rigid-body engines like Bullet Physics, impulse information is used to represent the movement state before and after a collision. Therefore, we input impulse information into deep learning models to simulate energy transfer in collisions. The physics engine temporarily converts the kinetic energy of the colliding objects into impulse information at the moment of collision, and then uses this information to adapt the velocity of the objects after the collision. Impulse information is also used in brittle fracture simulations to determine stress information using the BEM method.

To create training data (see left part of Figure 3), we assume the target shape exists in a zero-gravity scene where it will be destroyed. We place the target shape in the scene and a spherical space at its center. From sampling positions on the spherical space surface, we randomly fire balls towards the center. When a ball collides with the target shape,

we save the impulse information occurring on the shape’s surface as V^{raw} . We also save the shape generated by the destruction simulation as S^{part} , and convert it to a *geometrically-segmented signed distance function* (GS-SDF) format S^{gsdf} discussed later in Section 4.3.3.

Using the brittle fracture simulation module, we conduct a large number of simulations to create a training dataset \mathcal{D}_t for target $t \in \mathcal{T}$ with N_t^{cond} data pairs, where each data pair $(V_i^{\text{norm}}, S_i^{\text{gsdf}})$, and $\mathcal{D}_t = \{(V_i^{\text{norm}}, S_i^{\text{gsdf}}) \mid (V_i^{\text{norm}}, S_i^{\text{gsdf}}) \in \mathcal{D}_t, i = 1, \dots, N_t^{\text{cond}}\}$ consists of a normalized impulse information vector V_i^{norm} and a GS-SDF S_i^{gsdf} . For each data pair $(V_i^{\text{norm}}, S_i^{\text{gsdf}})$ in the training dataset \mathcal{D}_t , the seven-dimensional impulse information vector $V^{\text{raw}} = [p_x p_y p_z d_x d_y d_z I]$ contains the position ($\mathbf{p} \in \mathbb{R}^3$), direction ($\mathbf{d} \in \mathbb{R}^3$), and scalar value ($I \in \mathbb{R}$) of each impulse. All impulse information is normalized into V^{norm} with $[-1, 1]^7$.

To unify the size of the learning target shapes $\{S_t^{\text{origin}} \mid t \in \mathcal{T}\}$ treated in the space of the brittle fracture simulation module, the deep learning module, and the run-time process within the Euclidean space \mathbb{R}^3 and the voxel space \mathbb{V} , all shapes are normalized such that the longest length of their bounding boxes is 2. In the deep learning module, a voxel space \mathbb{V} of $[-1, 1]^{128 \times 128 \times 128}$ is created, and the center of the object is set to $(64, 64, 64)$ in the voxel space \mathbb{V} . The Euclidean space \mathbb{R}^3 from $(-1, -1, -1)$ to $(1, 1, 1)$ corresponds

to the voxel space \mathbb{V} from $(0, 0, 0)$ to $(128, 128, 128)$.

4.3. Network Architecture and Training Methodology

The main part of the learning process, as shown in Figure 3, is to create a set of conditional generative models $\{G_t \mid t \in \mathcal{T}\}$. Our generator G_t is specifically tailored to the target shape $\mathcal{S}_t^{\text{origin}}$ using the dataset \mathcal{D}_t .

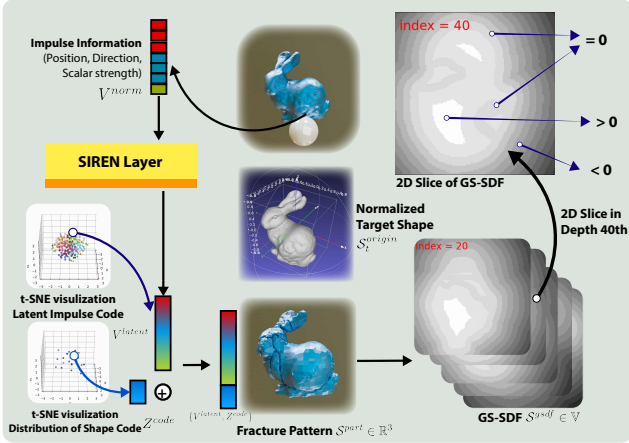


Figure 4. Design of latent impulse representation ($\mathbf{V}^{\text{latent}}, \mathbf{Z}$) and GS-SDF $\mathcal{S}^{\text{gsdf}}$.

4.3.1 Condition-to-voxel Generator and Fracture-pattern Discriminator

In our approach, the conditional generative model G_t learns a mapping from normalized impulse information \mathbf{V}^{norm} to a fracture pattern $\mathcal{S}^{\text{gsdf}}$ of target $t \in \mathcal{T}$: $G_t : \mathbf{V}^{\text{norm}} \rightarrow \mathcal{S}^{\text{gsdf}}$.

Following the concept of conditional GANs [24], as shown in the right part of Figure 3, we use a SIREN layer [36] as a position encoding layer E to transform the normalized impulse information \mathbf{V}^{norm} to the latent impulse code $\mathbf{V}^{\text{latent}}$: $E : \mathbf{V}^{\text{norm}} \rightarrow \mathbf{V}^{\text{latent}}$. We then learn a mapping from $\mathbf{V}^{\text{latent}}$ and the normal distribution code vector \mathbf{Z} to $\mathcal{S}^{\text{gsdf}}$ using our generator G_t : $\{\mathbf{V}^{\text{latent}}, \mathbf{Z}\} \rightarrow \mathcal{S}^{\text{gsdf}}$.

We adopt the basic generator design of five 3D transposed convolutional (ConvTranspose3D) layers, as proposed in [40] and widely accepted in subsequent CNN-based 3D voxel generative research [8]. Unlike existing voxel-based cGAN generators, our SIREN layer, latent impulse code $\mathbf{V}^{\text{latent}}$, and normal distribution code \mathbf{Z} are backpropagated during the training phase. For the fracture-pattern discriminator E , we also adopt the design of five 3D convolutional (Conv3D) layers, which are commonly used in voxel-based discriminators.

Traditional GANs and cGANs cannot guarantee sufficient stability for measuring the distance between the probability distributions of generated and real samples. To improve the

stability and performance of cGAN learning, we adopt the Wasserstein GAN (wGAN) [7] in our cGAN patch.

4.3.2 Latent Impulse Representation

To clarify, the concatenation of the latent impulse code and the normal distribution code $\{\mathbf{V}^{\text{latent}}, \mathbf{Z}\}$ represents the latent impulse representation in our research. As shown in Figures 3 and 4, the normalized impulse code $\mathbf{V}^{\text{norm}} \in [-1, 1]^7$ is a seven-dimensional vector, the latent impulse code $\mathbf{V}^{\text{latent}} \in [-1, 1]^{128}$ is a 128-dimensional vector, and the normal distribution code \mathbf{Z} is an eight-dimensional vector by default. With the mapping of the SIREN layer $E : \mathbf{V}^{\text{norm}} \rightarrow \mathbf{V}^{\text{latent}}$, we can obtain $\mathbf{V}^{\text{latent}}$ with higher-dimensional encoding.

Inspired by the autoencoder of DeepSDF [30], our normal distribution code \mathbf{Z} represents the shape code within the same condition, which is different from the random noise vector z in the general cGANs design. Our normal distribution code \mathbf{Z} is random at runtime but is stored and backpropagated during training, which means that the latent impulse code represents the latent space of the impulse condition, and the normal distribution code represents the latent space of multiple possible fracture patterns within the same impulse condition. Therefore, our latent impulse representation is specifically designed for the generative task of fracture patterns.

In Section 4.3.4, we will introduce the flow to use the impulse vector \mathbf{V}^{norm} and the training details for using the latent impulse representation $\{\mathbf{V}^{\text{latent}}, \mathbf{Z}\}$.

4.3.3 Geometrically Segmented Signed Distance Function (GS-SDF)

In our approach, following many experiences in 2D image deep learning research that utilize signed distance functions to learn segmentation information, we define a 3D *geometrically-segmented signed distance function* (GS-SDF) $\mathcal{S}^{\text{gsdf}}$ in a real coordinate space \mathbb{R}^3 .

The only difference between GS-SDF and the general signed distance function (SDF) is that GS-SDF contains multiple objects in one shape. As shown in Figure 4, the distance field inside the shape is positive, while the values outside the shape are negative, and the surface and the fracture surface are nearly 0.

In the voxel space for learning, we define $D(\mathbf{p})$ as the shortest Euclidean distance from the coordinate position \mathbf{p} to all boundary surfaces of the divided shape $\{S_r \mid S_r \subset \mathcal{S}^{\text{part}}, r = 1, \dots, N_{\text{regions}}\}$, where N_{regions} is the number of region divisions. In this case, the unsigned distance field (USDF) inside the learning target shape can be defined as: $D(\mathbf{p}) = \min(D_1(\mathbf{p}), D_2(\mathbf{p}), \dots, D_{N_{\text{regions}}}(\mathbf{p}))$ and $D_{\text{origin}}(\mathbf{p})$ can be specially treated as the Euclidean distance from the surface of the target shape $\mathcal{S}^{\text{origin}}$. By integrating external

and internal voxel space, we can define the GS-SDF $\mathcal{S}^{\text{gs sdf}}$ as $\{f^{\text{gs sdf}}(\mathbf{p}) \mid \mathbf{p} \in \mathbb{R}^3\}$ as follows (see Figure 4 upper right):

$$f^{\text{gs sdf}}(\mathbf{p}) = \begin{cases} D(\mathbf{p}), & \text{if } \mathbf{p} \in \mathcal{S}^{\text{part}} \\ -D_{\text{origin}}(\mathbf{p}). & \text{otherwise} \end{cases} \quad (1)$$

4.3.4 Objective and Learning Process Details

Notably, in our network architecture, our generator can be trained as a conditional autodecoder network, which means we can learn the mapping without cGAN patch according to this objective:

$$\mathcal{L}_{L_2}(G, E) = \mathbb{E}_{\mathbf{V}^{\text{latent}}, \mathcal{S}^{\text{gs sdf}}, \mathbf{Z}} [\|\mathcal{S}^{\text{gs sdf}} - G(E(\mathbf{V}^{\text{norm}}), \mathbf{Z}^{\text{code}})\|]. \quad (2)$$

Note that in the first step of objective of L_2 , $\mathbf{V}^{\text{latent}}$ will be updated, and we will attach each shape $\mathcal{S}_i^{\text{gs sdf}}$ with an initial random normal distribution code $\mathbf{Z}_i^{\text{code}}$, which means the backpropagation in the first step will change the distribution of the code \mathbf{Z}^{code} attached with the shape. As shown in the left part of Figure 5, the shape code of $\mathbf{Z}_i^{\text{code}}$ can be regarded as a shape code of $\mathcal{S}^{\text{gs sdf}}$.

cGAN is like a patch to improve the generalization of the network in our method. We then design the patch cGAN loss as follows:

$$\mathcal{L}_{\text{cGAN}}(G, D) = \mathbb{E}_{\mathbf{V}^{\text{latent}}, \mathbf{Z}^{\text{random}}} [\log(1 - D(G(\overline{\mathbf{V}^{\text{latent}}}, \mathbf{Z}^{\text{random}})))] + \mathbb{E}_{\mathcal{S}^{\text{gs sdf}}} [\log D(\mathcal{S}_{\text{closest}}^{\text{gs sdf}})]. \quad (3)$$

Note that in the objective of the cGAN patch, we will use a random normal distribution code $\mathbf{Z}^{\text{random}}$, lock the $\mathbf{V}^{\text{latent}}$, and search for the latent impulse representation with the closest Euclidean distance to its fracture pattern $\{\mathbf{V}_{\text{closest}}^{\text{latent}}, \mathbf{Z}_{\text{closest}}\} \rightarrow \mathcal{S}_{\text{closest}}^{\text{gs sdf}}$ in the dataset. During the learning of the cGAN patch, we will generate new noise $\mathbf{Z}^{\text{random}}$ and train the objective above in Equation (3). We can then apply the Wasserstein GAN (wGAN) loss into our framework. The mathematical definition of the objective is:

$$\mathcal{L}_{\text{wGAN}}(G, D) = \mathbb{E}_{\mathbf{Z}^{\text{random}} \sim P_G} [D(G(\overline{\mathbf{V}^{\text{latent}}}, \mathbf{Z}^{\text{random}}))] - \mathbb{E}_{\mathbf{Z}^{\text{random}} \sim P_{\mathcal{S}^{\text{gs sdf}}}} [D(\mathcal{S}_{\text{closest}}^{\text{gs sdf}})]. \quad (4)$$

Note that P_G represents the probability distribution of the ‘‘fake’’ samples generated by G with the random noise normal distribution code $\mathbf{Z}^{\text{random}}$, and $P_{\mathcal{S}^{\text{gs sdf}}}$ represents the probability distribution of the ‘‘real’’ samples that are searched by finding the latent impulse representation with the closest Euclidean distance. Significantly, searching for the closest random $\mathbf{Z}^{\text{random}}$ enables latent space exploration of the latent impulse representation condition space, which makes

our discriminator a conditional one. After these three improvements to the loss function in our framework, we can summarize our final objective here:

$$G^* = \arg \min_G \max_D \mathcal{L}_{\text{wGAN}}(G, D) + \mathcal{L}_{L_2}(G, E). \quad (5)$$

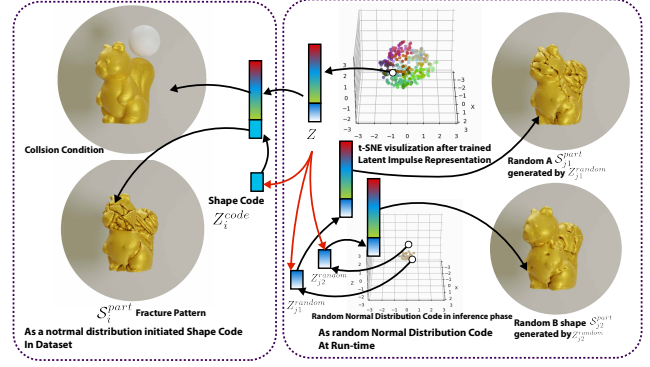


Figure 5. Difference of normal distribution code between the learning process and run-time: During the first step of the objective, \mathbf{Z} is treated as $\mathbf{Z}_i^{\text{code}}$, which is first initialized in the normal distribution and then connected to a specific $\mathcal{S}_i^{\text{part}}$ in the dataset \mathcal{D} . However, at run-time, the normal distribution code \mathbf{Z} is treated as a random noise $\mathbf{Z}^{\text{random}}$. With different $\mathbf{Z}_{j1}^{\text{random}}$ or $\mathbf{Z}_{j2}^{\text{random}}$, we can get totally different shapes of $\mathcal{S}_{j1}^{\text{part}}$ or $\mathcal{S}_{j2}^{\text{part}}$. Our first objective is to learn the representation of the GS-SDF, and our second objective is to improve the random code of $\mathbf{Z}^{\text{random}}$ to represent a reasonable fracture pattern.

4.3.5 Inference Phase

During the inference phase, we generate a new random normal distribution code $\mathbf{Z}^{\text{random}}$ and accept a normalized impulse code \mathbf{V}^{norm} from the run-time process, as shown in Figure 5. After applying the mapping $G(E(\mathbf{V}^{\text{norm}}), \mathbf{Z}^{\text{random}})$, which takes \mathbf{V}^{norm} to $\mathcal{S}^{\text{gs sdf}}$, we obtain the predicted fracture pattern $\mathcal{S}^{\text{gs sdf}}$.

5. Run-time Process

During the run-time process shown in Figure 6, the run-time rigid body engine module executes rigid body simulations using Bullet Physics. If a collision of the target shape $\mathcal{S}_t^{\text{origin}}$ is detected, the impulse information \mathbf{V}^{raw} is relayed to the conditional generator G_t of the fracture pattern prediction module, which was trained by the deep learning module during the learning process. The predicted fractured pattern $\mathcal{S}_j^{\text{gs sdf}}$ is then efficiently converted into a 3D segmented shape $\mathcal{S}_j^{\text{part}}$ and reintroduced to the rigid body simulation. The rigid body simulation continues by replacing the original model $\mathcal{S}_t^{\text{origin}}$ with the reconstructed destruction pattern $\mathcal{S}_j^{\text{part}}$ ($j = 1, \dots, N_{\text{test}}$, where N_{test} represents the number of test times.)

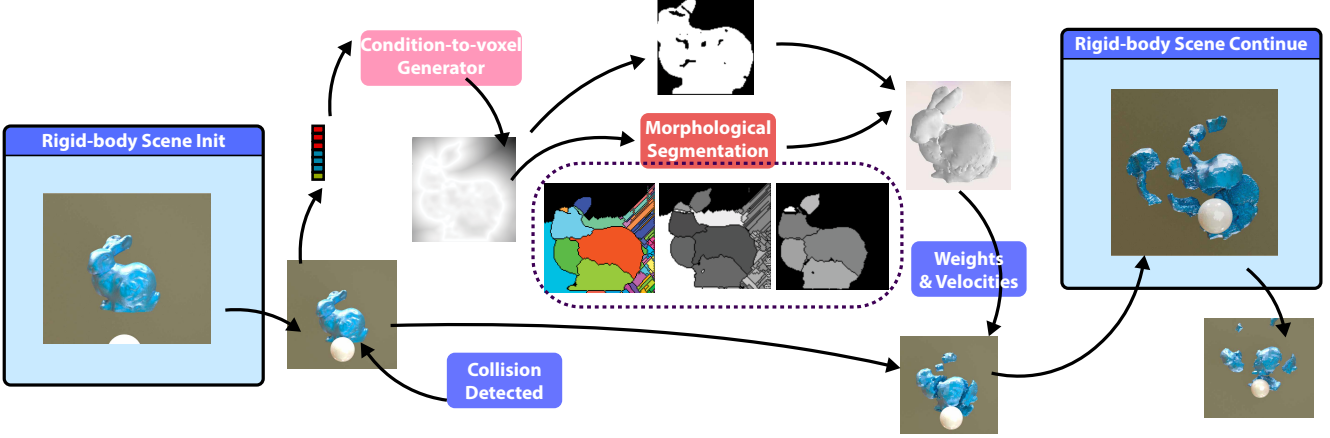


Figure 6. Flowchart of the run-time process: After receiving the condition-to-voxel generator from the learning process in Figure 3, the rigid body system can predict the shape for the fracture scene. Once a collision occurs and the impulse is over the threshold, we provide a \mathbf{V}^{norm} to the condition-to-voxel generator G . After receiving the prediction of voxel data $\mathcal{S}_j^{\text{ssdf}}$, we pre-process and apply morphological segmentation to the data. We then pass the segmentation results to post-process and add the weights and velocity to the fragments shapes $\mathcal{S}^{\text{part}}$. The old rigid-body object representing $\mathcal{S}^{\text{origin}}$ is removed, and new shapes $\mathcal{S}^{\text{part}}$ are treated as rigid-bodies and continue the rigid-body simulation.

5.1. Collision in Pre-processing Module and Prediction Module

During the run-time process, the rigid body simulation checks for collisions for every frame. If a collision is detected, all the impulses of the target shape $\mathcal{S}_t^{\text{origin}}$ within that frame are accumulated. If the cumulative impulse value reaches or exceeds 10Ns per 4ms, a raw impact information $\mathbf{V}^{\text{raw}} \in \mathbb{R}^7$ is extracted. Concurrently, the velocity and mass $\{\mathbf{v}^{\text{origin}}, m^{\text{origin}}\}$ of the target shape $\mathcal{S}_t^{\text{origin}}$ are stored. The method to create normalized impact information \mathbf{V}^{norm} from \mathbf{V}^{raw} is detailed in Section 4.2. Following this, the fracture pattern $\mathcal{S}_j^{\text{ssdf}}$ for target t is predicted using the conditional generative model G_t with the condition \mathbf{V}^{norm} .

To prepare for the reconstruction process, we first create a mask M_j from the GS-SDF $\mathcal{S}_j^{\text{ssdf}}$ by filtering the values greater than or equal to 0. During the procedure in Section 5.2, an unsigned distance field (USDF) $\mathcal{S}_j^{\text{usdf}} \in [0, 1]^{128 \times 128 \times 128}$ is generated by multiplying the values of $\mathcal{S}_j^{\text{ssdf}}$ less than 0 by -1.

5.2. Morphological Segmentation

To reconstruct the destruction pattern in 3D, it is essential to segment all fragment regions as individual entities. Morphological segmentation is an algorithm-based method that provides unique labels to each identical fragment, similar to instance segmentation. It does not focus on labeling all fragments with a single identifier. Traditional 3D cell segmentation [39] transforms 3D medical imaging data into a 3D distance field and applies morphological segmentation algorithms to assign different labels to each 3D region.

Through the prediction of the generator and the prepro-

cessing in our approach, an unsigned distance field (USDF) $\mathcal{S}_t^{\text{usdf}}$ is produced as output. The USDF is then subjected to morphological segmentation, and each segmented region is assigned a unique label. All uniquely labeled shape regions are reconstructed into a 3D mesh using an isosurface extraction algorithm such as marching cubes, forming the mesh $\mathcal{S}_t^{\text{part}}$ that feeds into the rigid body simulation engine.

The morphological segmentation method adopted here is an algorithm often employed for cell division in 3D medical images. For 3D voxels, the algorithm starts at the lowest value; as thresholds rise and the region broadens, connected spaces are scanned to determine segmented areas. Using the USDF $\mathcal{S}_t^{\text{usdf}}$ generated in Section 5.1, segmentation is executed cell-by-cell by raising the threshold in 0.04 increments. All segmented areas are eventually labeled distinctively, and this data is stored. The run-time process utilizes the MorphoLibJ library [19] shown in Figure 6.

5.3. Reconstruction and Post-processing

Subsequently, the target shape region mask M_j described in Section 5.1 is compared with the fractured pattern segmentation $\mathcal{S}_j^{\text{morph}}$ from Section 5.2. Only labels corresponding to the mask M_j represent the definitive destruction pattern regions.

For every label in the fractured pattern segmentation, the fragment shape region $\{\mathcal{S}_r^{\text{label}} \mid \mathcal{S}_r^{\text{label}} \in \mathcal{S}^{\text{morph}}, r = 1, \dots, N_{\text{regions}}\}$ is converted into mesh data $\{\mathcal{S}_r^{\text{mesh}} \mid \mathcal{S}_r^{\text{mesh}} \in \mathcal{S}^{\text{part}}, r = 1, \dots, N_{\text{regions}}\}$ using the marching cubes algorithm. The mass of each fragment is determined based on its size relative to the original shape. Using the velocity of the shape $\mathbf{v}^{\text{origin}}$ stored before being replaced in Section 5.1, the

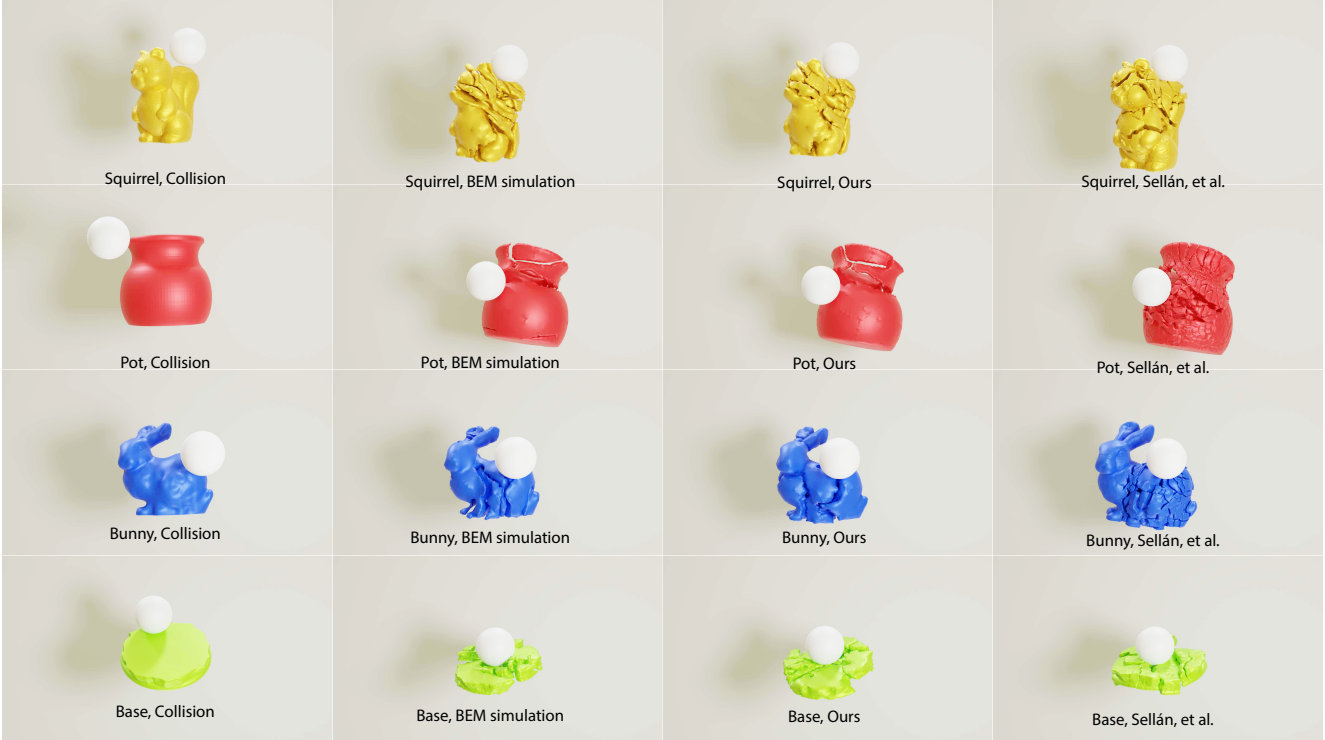


Figure 7. Comparison between the simulation results, results by Sellán et al., and fracture shape prediction results using deep learning. Left to right: Input collision condition, Brittle fracture simulation results, Results of our method, Results by Sellán et al. [35]. Top to bottom row: Squirrel, Bunny, Pot, Base. Note that our results were generated by two random normal distribution codes and we picked one, which is the process shown in the run-time process in Figure 5. For the results by Sellán et al. [35], we computed the system with 6000 cages and from 5 to 60 modes and picked the best visualization of all the test cases.

velocity $\{v_r \mid v_r = v^{\text{origin}}\}$ is distributed evenly to the newly formed fragment rigid-body shapes as rigid-body information.

In the concluding steps, the original pre-destruction shape is eliminated. The reformed fragment shapes, with their mass m_r and velocity v_r , are integrated as rigid bodies into Bullet Physics. The destruction animation is completed by computing subsequent frames as the rigid-body simulation.

6. Experimental Results and Discussion

6.1. Dataset and Implementation

In all experiments, we used the shape data scanned by Thing10K [41]. We selected four models from Thing10K: Pot (Thing ID:12120), Bunny (Thing ID:240197), and Squirrel (Thing ID:11705), and Base (Thing ID:17204). For each model, we conducted both the learning and run-time processes. These results are presented in this paper, and we also performed comparative experiments with the simulation results of Hahn et al. [10] and Sellán et al. [35]. The experiments showed that our method can be stably applied to watertight meshes of many shape types.

6.2. Creation of Learning Data and Deep Learning

Using the brittle fracture simulation module described in Figure 3, calculations were carried out for five days on four PCs with Ryzen 9 5950X CPUs. For each of the four learning target shapes, Pot, Bunny, Squirrel, and Base we conducted 200-frames destruction experiments in the scene environment introduced in Section 4.2, colliding 600 times and collecting that data. As a result, we calculated 600 sets of input and output learning data for each of Pot, Bunny, and Squirrel. We used 500 sets in the learning process, and 100 sets for testing in Figure 7, Figure 9 and Figure 8. The impulse of position, direction, and strength used for testing is not included in the learning process.

During the learning process, we adopt a previous version of implementing wGAN in [1], but the wGAN-GP in [7], which can be more simply applied to our learning objective. The training time for all learning target shapes was 1000 epochs, since we have few data compared with large datasets. For better stability verification of the model, we only set the batch size as 1, which makes us take an average of 24.4 hours to complete each learning process. Also, when updating the

generator’s parameters, we update the two-step objectives individually.



Figure 8. Fracture surface comparison among BEM simulation, our method, and Sellán et al.’s: All the results were generated by similar collision conditions. The results of BEM simulation and our method represent a complex fracture shape with similar characteristics. Note that the result of Sellán et al.’s method was generated at a resolution of 6000 cages with 60 modes.

6.3. Comparison of Brittle Fracture Shape Prediction Results with Simulation Results

Figure 7 shows that our results are similar to brittle fracture simulation results in terms of destruction patterns, global complexity, and fracture surface shapes. Compared to Sellán et al., our method occasionally generates fewer fracture shapes, but the patterns are more realistic and plausible. Our method can predict the numerous fragments around the impact sites and the overall fracture pattern, and it prevents the emergence of smaller, similar convex hull shapes in these situations.

Figure 8 shows that our fracture animation can produce complex shapes and impressive visual impacts for more complex fracture surfaces. Sellán et al.’s results depend on the parameters of cages and modes. Sellán et al. use a cage-based structure to generate fracture surfaces, and the number of cage elements determines the resolution and complexity of the generated patterns. The mode parameter generates pre-fracture patterns and reflects them in the interactive fracture system. In our experiments, we generated fragments that reproduce Sellán et al.’s results using 6000 cage elements and mode values ranging from 5 to 50. The rightmost Pot example in Figure 7 shows that using a high number of modes (more than 50) in Sellán et al.’s system results in an unrealistic fracturing process, producing numerous fragments.

Our method focuses on capturing the characteristics of instantaneous brittle fracture processes and the relationship between the collision situation and the pre-fractured pattern. Therefore, we do not consider re-fracture of already broken shapes. Table 1 summarizes the benefits and drawbacks of each method. Our method is faster than BEM simulation but cannot reach real time, making it a trade-off selection between BEM simulation and real-time techniques for generating fracture animation.

	Run-time	Reality	Stability
BEM [10]	20 mins - 5 hours	Realistic	High
Our method	5-10 sec.	High	Middle
Sellán et al. [35]	Real-time	Middle	High

Table 1. Qualitative comparison among BEM simulation, our methods and Sellán et al.’s. Our method is a trade-off selection between BEM simulation and real-time technique to generate fracture animation.

6.4. Ablation Study

We conducted an ablation study to assess the efficiency of our wGAN update module, latent impulse representation, and varying dimensions of the normal distribution code.

We first compare our method with an enhanced 3D-Pix2pix based on Pix2Pix [15], where all 2D convolution layers are replaced with 3D convolution layers. Impulse information is encoded into voxels by appending the impulse scalar value to the voxel position. This method can produce fractured shapes similarly. However, as shown in Figure 9 (“Pix2pix”), it struggles to represent fracture patterns similar to simulations when collisions occur at the Squirrel’s head position. Models without normal distribution code use the latent impulse code as their generator input, but without latent impulse representation. Models without normal distribution code (“w/o Normal Distribution Code”) and Pix2pix

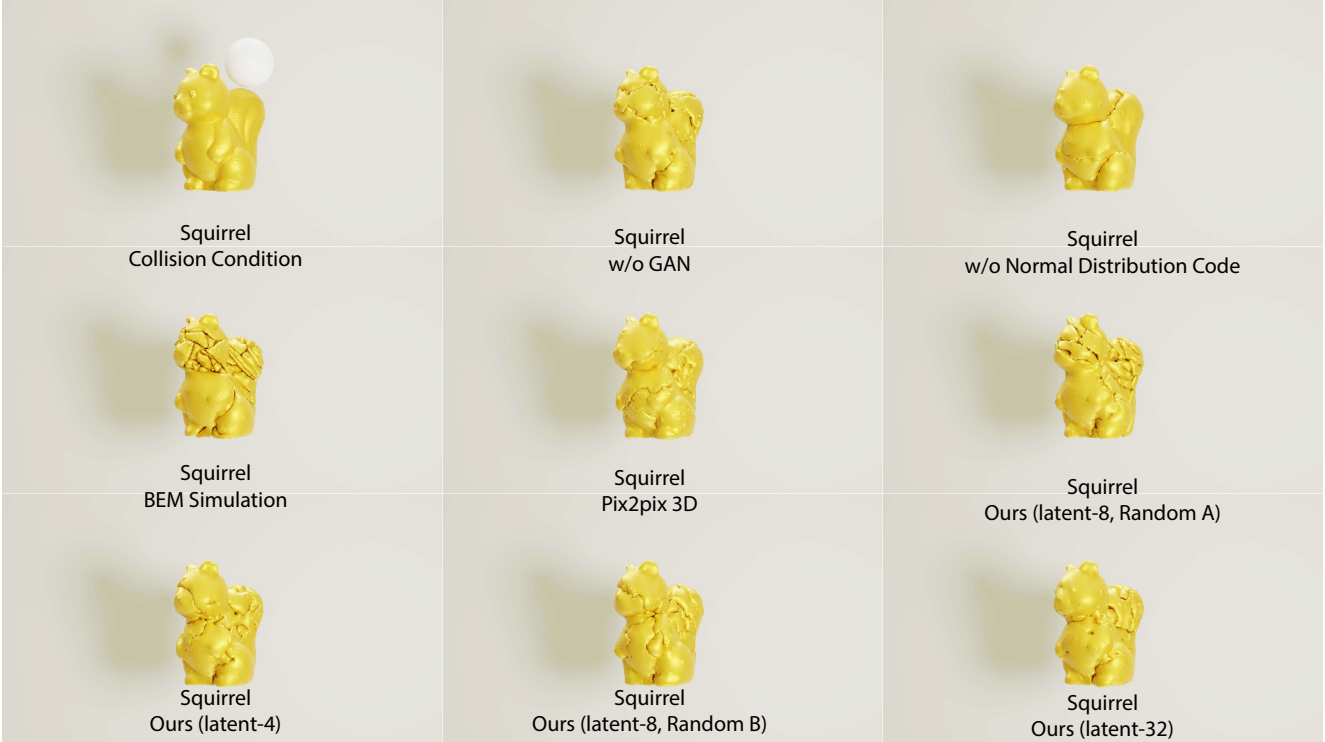


Figure 9. Results of the ablation study: We chose the same input as the Squirrel case in Figure 7 and tested the case with several networks individually. Note that the input of the test case is a ball collision with the Squirrel’s head. We expect the models to learn the high-density fragments surrounding the head of the Squirrel, just like the result of BEM simulation. Ours (latent-8, latent-4, latent-32): The proposed models with an eight-dimensional, four-dimensional, and 32-dimensional normal distribution code. Pix2pix: The 3D extended version of Pix2pix [15]. w/o GAN: The model only learns the first step of the objective in Section 4.3. w/o Normal Distribution Code: The model without normal distribution code.

(“Pix2pix”) can only generate limited maps, which are difficult to correlate with the simulated fracture pattern and collision scenario.

A model that only employs the first objective step, without integrating a GAN-based objective, alongside models equipped with a GAN-based objective and a four-dimensional normal distribution code (“latent-4” in Figure 9), can perform well in the collision scenario occurring at the Squirrel’s head position. Interestingly, models with eight-dimensional (“latent-8”) and 32-dimensional (“latent-32”) normal distribution codes give a more stable and better performance as shown in Figure 9 and also in Figure 10.

As shown in Figure 5, during run-time, we incorporate a random normal distribution code. This means that not only “Random A” but also “Random B” in Figure 9 are produced. Nevertheless, both efficiently reflect the “Collision on Head” outcome in the given context. Furthermore, we computed and collected the L_2 loss across the training phase for all models, as shown in the first step of the objective in Section 4.3. The L_2 loss between prediction and ground truth means the ability to reproduce the resolution of the fractured shapes.

It’s noteworthy that most models with GAN-based objectives tend to become unstable as the discriminator and the generator engage in adversarial learning. As evident in Figure 10, our techniques using eight-dimensional and 32-dimensional normal distribution codes achieved higher accuracy by the end of the learning, while the latent-4 model lagged behind, showcasing reduced accuracy. Although the model without a GAN-based objective registers higher accuracy, it also misses the stability, especially when encountering a random normal distribution code, in contrast to other GAN-based models. Additionally, even when employing an eight-dimensional normal distribution code for our latent impulse representations, we utilized minimal data for training the models. This suggests that the model can still be efficiently trained using a higher dimension of the normal distribution code. Going forward, a deeper dive into hyperparameter tuning, focusing on neural network size, dataset magnitude, and dimensions of both latent impulse code and normal distribution code, would be beneficial.

	BEM [10]	Our method						Sellán et al.[35]	
	Sim.	Data Gen.	Train.	Pred.	Recon.	Others.	Run-time	Mode Gen.	Impact Proj.
Pot	12.4 mins	2 days	20.1 hours	1.30s	0.72s	1.24s	3.26s	38.8 mins	0.005s
Bunny	46.3 mins	4 days	38.0 hours	1.47s	1.20s	5.71s	8.38s	34.4 mins	0.002s
Base	16.4 mins	2 days	28.3 hours	0.80s	2.69s	6.70s	10.19s	17.0 mins	0.001s
Squirrel	32.1 mins	4 days	31.3 hours	1.42s	1.90s	2.41s	5.73s	16.3 mins	0.004s
Mean	26.8 mins	3 days	29.4 hours	1.25s	1.63s	4.02s	6.89s	26.6 mins	0.003s

Table 2. Comparison of computation times in Figure 7: Sim.: Time required to generate a single simulation. Data Gen.: Time required to perform 600 simulations on the two machines described in Section 6.2. Train.: Network training time. Pred.: Time required to predict a single fracture pattern during run-time. Recon.: Time required to reconstruct a three-dimensional fracture shape for a single fracture pattern during run-time. Others: Time required to pre-process and post-process at run-time. Run-time: Time required to produce a fracture animation during run-time. Mode Gen.: Time required to pre-compute force and generate the fracture modes. Impact Proj.: Time required to project the fracture shape based on force information during a collision from the generated parent fracture pattern.

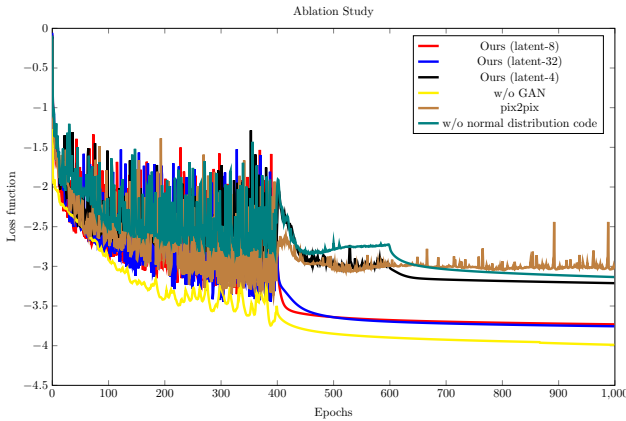


Figure 10. Ablation study graph: We calculated and collected the L_2 loss while training the models shown in Figure 9. The L_2 loss represents the first step of the objective in Section 4.3. It measures the ability of the model to reproduce the resolution of the fractured shapes. The GAN-based models struggled to reduce the error at first. Ours (latent-8, latent-4, latent-32): The proposed models with an eight-dimensional, four-dimensional, and 32-dimensional normal distribution code. Pix2pix: The 3D extended version of Pix2pix [15]. w/o GAN: The model only learns the first step of the objective in Section 4.3. w/o Normal Distribution Code: The model without normal distribution code.

6.5. Destruction Animation Generation Time during Run-time

Sellán et al. took an average of 26.6 mins to create 5-30 destruction patterns for one shape with 6000 cages and 0.003 seconds to adapt the destruction shape at run-time. Our method took an average of 3 days on two machines to perform 600 destruction simulations. We trained a generator on 480 patterns for one shape and could generate a destruction pattern for any collision in an average of 6.89 seconds at run-time.

Our deep learning-based method generated visually close results to the brittle fracture simulation within an average reasonable calculation time of 6.89 seconds, compared to the average calculation time of 26.8 minutes for the brittle fracture simulation.

6.6. Limitations and Future Work

Our method faces challenges in ensuring industry usability, improving stability during the prediction and segmentation process, maintaining appearance post-fracturing, and implementing our technique for higher-resolution target shapes.

Even though our prediction can rapidly produce fracture patterns, it is hard to reach the real-time level as the other real-time fracture animation techniques, such as Sellán et al. [35]. As indicated by the reconstruction time costs for “Recon” and “Others” in Table 2, our method currently struggles to generate fractures within a second. Achieving an interactive network-based fracture animation system in real-time would be a significant advancement in industry techniques.

Furthermore, our system requires training a generative model specific to each shape and physical material. This poses an industrial application challenge, given the lack of generalizability in our method for various shapes and materials without the need for re-training.

Unstable predictions arise occasionally due to noise during the prediction and segmentation phase, as well as the unpredictable learning process.

In the comparison shown between “Squirrel, Ours” and “Squirrel, Sellán et al.” in Figure 7, our method, in contrast to Sellán et al., not only generates the fractured surface of the object but also remeshes non-fractured surface area of the original object, as observed in the “Squirrel Nose” and “Squirrel Ear”. This issue causes a drawback of losing details.

Lastly, enhancing the resolution of voxel data poses difficulties due to the increased inference time of networks and morphological segmentation. This is further investigated when we try to augment network size and segmentation to

refine prediction result details.

Nonetheless, due to the present challenges above, several enhancements are needed for our approach:

- Expand our deep-learning fracture animation system to accommodate varied attributes, including different shapes and diverse materials.
- Incorporate a network-driven mesh-reconstruction method coupled with swifter 3D segmentation techniques based on the network.
- Develop an improved 3D representation of manifold fracture shapes and design a network architecture attuned to this representation.
- Address the scalability challenge of applying our learning-based method to expansive fracture scenes containing numerous fragments. A solution must be able to predict solely surface fracturing while dynamically adapting to structured shapes.
- Explore additional deep learning methodologies, such as diffusion models and graph neural networks, which may be seamlessly integrated into the generative fracture generation task.
- Combine our system with a module that allows artistic control.

7. Conclusion

In this paper, we introduced the prior application of a deep learning-based fracture system, defining the task of 3D destruction shape generation.

Our proposed method predicts brittle fracture shapes using a 3D conditional adversarial generative network tailored for rigid body simulations. Experimental outcomes show that, compared to traditional methods at run-time, our deep learning approach can generate more intricate and lifelike destruction forms within a practical computation time frame.

References

- [1] Martin Arjovsky, Soumith Chintala, and Léon Bottou. Wasserstein generative adversarial networks. In *Proc. 34th International Conference on Machine Learning*, pages 214–223. JMLR.org, 2017. 9
- [2] Franz Aurenhammer and Rolf Klein. Voronoi diagrams. In *Handbook of Computational Geometry*, chapter 5, pages 201–290. North-Holland, Amsterdam, 2000. 3
- [3] Zhaosheng Bao, Jeong-Mo Hong, Joseph Teran, and Ronald Fedkiw. Fracturing rigid materials. *IEEE Transactions on Visualization & Computer Graphics*, 13(2):370–378, 2007. 2
- [4] Floyd M Chitalu, Qinghai Miao, Kartic Subr, and Taku Komura. Displacement-correlated XFEM for simulating brittle fracture. *Computer Graphics Forum*, 39(2):569–583, 2020. 2
- [5] Erwin Coumans. Bullet physics simulation. In *ACM SIGGRAPH 2015 Courses*. ACM, New York, NY, USA, 2015. 2, 4
- [6] Linxu Fan, Floyd M Chitalu, and Taku Komura. Simulating brittle fracture with material points. *ACM Transactions on Graphics (TOG)*, 41(5):1–20, 2022. 1, 2
- [7] Ishaan Gulrajani, Faruk Ahmed, Martin Arjovsky, Vincent Dumoulin, and Aaron C. Courville. Improved training of Wasserstein GANs. In *Advances in Neural Information Processing Systems*, pages 5769–5779. Curran Associates, Inc., Red Hook, NY, USA, 2017. 6, 9
- [8] Kamal Gupta, Susmija Jabbireddy, Ketul Shah, Abhinav Shrivastava, and Matthias Zwicker. Improved modeling of 3D shapes with multi-view depth maps. In *2020 International Conference on 3D Vision (3DV)*, pages 71–80. IEEE Computer Society, Los Alamitos, CA, USA, 2020. 3, 6
- [9] David Hahn and Chris Wojtan. High-resolution brittle fracture simulation with boundary elements. *ACM Trans. Graph.*, 34(4), 2015. 2, 3
- [10] David Hahn and Chris Wojtan. Fast approximations for boundary element based brittle fracture simulation. *ACM Trans. Graph.*, 35(4), 2016. 1, 2, 3, 4, 9, 10, 12
- [11] Jeffrey Hellrung, Andrew Selle, Arthur Shek, Eftychios Sifakis, and Joseph Teran. Geometric fracture modeling in Bolt. In *SIGGRAPH 2009: Talks*. ACM, New York, NY, USA, 2009. 3
- [12] Yuhang Huang, Yonghang Yu, and Takashi Kanai. Predicting brittle fracture surface shape from a versatile database. *Computer Animation and Virtual Worlds*, 30(6):e1865, 2019. 3
- [13] Takashi Imagire, Henry Johan, and Tomoyuki Nishita. A fast method for simulating destruction and the generated dust and debris. *The Visual Computer*, 25(5-7):719–727, 2009. 2
- [14] Takashi Imagire, Henry Johan, and Tomoyuki Nishita. A method to control the shape of destroyed objects in destruction simulation. *Journal of the Institute of Image Electronics Engineers of Japan*, 38(4):449–458, 2009. 2
- [15] Phillip Isola, Jun-Yan Zhu, Tinghui Zhou, and Alexei A. Efros. Image-to-image translation with conditional adversarial networks. In *Proc. IEEE Conference on Computer Vision and Pattern Recognition*, pages 5967–5976. IEEE Computer Society, Los Alamitos, CA, USA, 2017. 10, 11, 12
- [16] Nikolas Lamb, Sean Banerjee, and Natasha Kholgade Banerjee. DeepJoin: Learning a joint occupancy, signed distance, and normal field function for shape repair. *ACM Trans. Graph.*, 41(6), 2022. 4
- [17] Nikolas Lamb, Sean Banerjee, and Natasha K Banerjee. MendNet: Restoration of fractured shapes using learned occupancy functions. *Computer Graphics Forum*, 41(5):65–78, 2022.
- [18] Nikolas Lamb, Cameron Palmer, Benjamin Molloy, Sean Banerjee, and Natasha Kholgade Banerjee. Fantastic breaks: A dataset of paired 3D scans of real-world broken objects and their complete counterparts. In *Proc. IEEE/CVF Conference on Computer Vision and Pattern Recognition*, pages 4681–4691, 2023. 4
- [19] David Legland, Ignacio Arganda-Carreras, and Philippe Andrey. MorphoLibJ: Integrated library and plugins for mathematical morphology with ImageJ. *Bioinformatics*, 32(22):3532–3534, 2016. 8

- [20] Ning Liu, Xiaowei He, Sheng Li, and Guoping Wang. Meshless simulation of brittle fracture. *Computer Animation and Virtual Worlds*, 22(2-3):115–124, 2011. 3
- [21] A. Mandal, P. Chaudhuri, and S. Chaudhuri. Remeshing-free graph-based finite element method for fracture simulation. *Computer Graphics Forum*, 42(1):117–134, 2023. 2
- [22] Oleg Mazarak, Claude Martins, and John Amanatides. Animating exploding objects. In *Proc. Graphics Interface*, pages 211–218. Morgan Kaufmann Publishers Inc., San Francisco, CA, USA, 1999. 2
- [23] Ben Mildenhall, Pratul P. Srinivasan, Matthew Tancik, Jonathan T. Barron, Ravi Ramamoorthi, and Ren Ng. NeRF: Representing scenes as neural radiance fields for view synthesis. In *Proc. 16th European Conference on Computer Vision Part I*, pages 405–421. Springer-Verlag, Berlin, Heidelberg, 2020. 4
- [24] Mehdi Mirza and Simon Osindero. Conditional generative adversarial nets. *arXiv preprint arXiv:1411.1784*, 2014. 2, 6
- [25] Matthias Müller, Nuttapon Chentanez, and Tae-Yong Kim. Real time dynamic fracture with volumetric approximate convex decompositions. *ACM Trans. Graph.*, 32(4), 2013. 1, 3
- [26] Michael Neff and Eugene Fiume. A visual model for blast waves and fracture. In *Proc. Graphics Interface*, pages 193–202. Morgan Kaufmann Publishers Inc., San Francisco, CA, USA, 1999. 3
- [27] Alan Norton, Greg Turk, Bob Bacon, John Gerth, and Paula Sweeney. Animation of fracture by physical modeling. *The Visual Computer*, 7(4):210–219, 1991. 2
- [28] James F. O’Brien and Jessica K. Hodgins. Graphical modeling and animation of brittle fracture. In *Proc. ACM SIGGRAPH ’99*, pages 137–146. ACM, New York, NY, USA, 1999. 2
- [29] James F. O’Brien, Adam W. Bargteil, and Jessica K. Hodgins. Graphical modeling and animation of ductile fracture. *ACM Trans. Graph.*, 21(3):291–294, 2002. 2
- [30] Jeong Joon Park, Peter Florence, Julian Straub, Richard Newcombe, and Steven Lovegrove. DeepSDF: Learning continuous signed distance functions for shape representation. In *Proc. IEEE/CVF Conference on Computer Vision and Pattern Recognition*, pages 165–174, 2019. 4, 6
- [31] PhysXSDK. NVIDIA PhysX SDK. <https://developer.nvidia.com/physx-sdk>. Accessed: 2nd October, 2023. 3
- [32] Saty Raghavachary. Fracture generation on polygonal meshes using Voronoi polygons. In *ACM SIGGRAPH 2002 Conference Abstracts and Applications*, pages 187–187. ACM, New York, NY, USA, 2002. 3
- [33] Sara C. Schwartzman and Miguel A. Otaduy. Fracture animation based on high-dimensional Voronoi diagrams. In *Proc. 18th ACM SIGGRAPH Symposium on Interactive 3D Graphics and Games*, pages 15–22. ACM, New York, NY, USA, 2014. 1, 3
- [34] Silvia Sellán, Yun-Chun Chen, Ziyi Wu, Animesh Garg, and Alec Jacobson. Breaking bad: A dataset for geometric fracture and reassembly. In *Advances in Neural Information Processing Systems*, pages 38885–38898. Curran Associates, Inc., Red Hook, NY, USA, 2022. 4
- [35] Silvia Sellán, Jack Luong, Leticia Mattos Da Silva, Aravind Ramakrishnan, Yuchuan Yang, and Alec Jacobson. Breaking good: Fracture modes for realtime destruction. *ACM Trans. Graph.*, 42(1), 2023. 2, 3, 4, 9, 10, 12
- [36] Vincent Sitzmann, Julien Martel, Alexander Bergman, David Lindell, and Gordon Wetzstein. Implicit neural representations with periodic activation functions. In *Advances in Neural Information Processing Systems*, pages 7462–7473. Curran Associates, Inc., Red Hook, NY, USA, 2020. 2, 4, 6
- [37] Jonathan Su, Craig Schroeder, and Ronald Fedkiw. Energy stability and fracture for frame rate rigid body simulations. In *Proc. ACM SIGGRAPH/Eurographics Symposium on Computer Animation*, pages 155–164. ACM SIGGRAPH / Eurographics Association, 2009. 3
- [38] Demetri Terzopoulos and Kurt Fleischer. Modeling inelastic deformation: Viscoelasticity, plasticity, fracture. *SIGGRAPH Comput. Graph.*, 22(4):269–278, 1988. 2
- [39] Andong Wang, Qi Zhang, Yang Han, Sean Megason, Sahand Hormoz, Kishore R Mosaliganti, Jacqueline CK Lam, and Victor O.K. Li. A novel deep learning-based 3D cell segmentation framework for future image-based disease detection. *Scientific Reports*, 12(1):342, 2022. 8
- [40] Jiajun Wu, Chengkai Zhang, Tianfan Xue, Bill Freeman, and Josh Tenenbaum. Learning a probabilistic latent space of object shapes via 3D generative-adversarial modeling. In *Advances in Neural Information Processing Systems*, pages 82–90. Curran Associates, Inc., Red Hook, NY, USA, 2016. 3, 6
- [41] Qingnan Zhou and Alec Jacobson. Thingi10k: A dataset of 10,000 3D-printing models. *arXiv preprint arXiv:1605.04797*, 2016. 4, 9

A. Supplemental Material

We have analyzed the generator models of Base and Squirrel, as utilized to generate the examples in Figure 7.

For the Base generator shown in Figure 11, we examined scenes of balls shot in different directions. Our Base generator was able to create fracture patterns that are sensitive to the impact position, producing reasonably complicated and realistic fracture shapes appropriate for each distinct collision position. Nonetheless, the BEM simulation offers more realism by preserving large fragments on the side opposite the collision.

For the Squirrel generator in Figure 12, we explored scenes with balls shot in a similar direction but with varying speeds. In this figure, Squirrel Collision B represents the fastest shot, while Squirrel Collision C is the slowest. Squirrel Collision B, where the ball hits both the tail and head of the squirrel, exhibits fractures in both areas. Conversely, Squirrel Collision A shows fractures only in the tail, where it was hit, while Squirrel Collision C displays fractures in the head. However, the random instance from our Squirrel generator did not replicate the complicated fractured shape seen in the BEM Simulation for the test case shown in Figure 12.



Figure 11. In the comparison for the Base, the varying collision directions are presented from left to right: case A, case B, and case C. Vertically, from top to bottom, we show the initial frame of each scene, followed by our method and then the BEM simulation. All selected frames are taken post-collision.

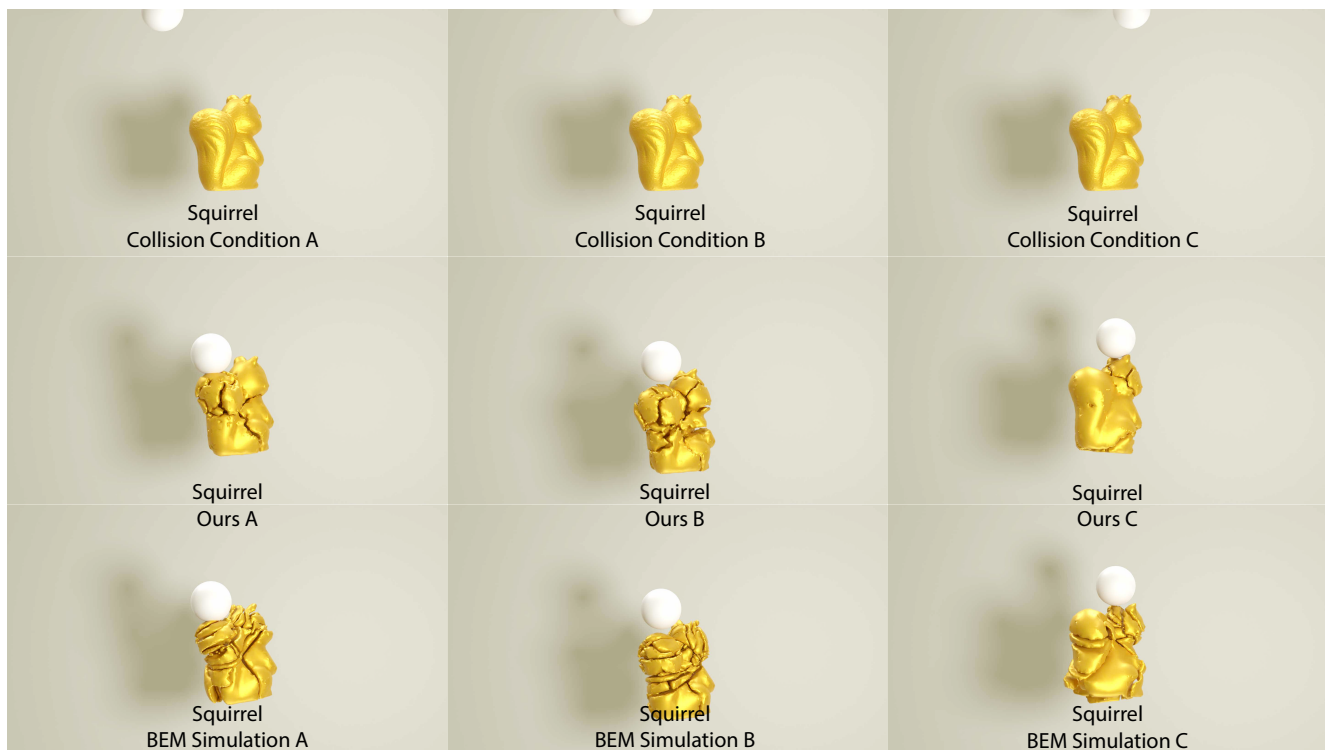


Figure 12. For the Squirrel comparison, which examines impulses from varying strengths but similar directions, the sequence from left to right is: case A, case B, and case C. Again, from top to bottom, we display the initial frame for each scene, our method, and the BEM simulation. Notably, Squirrel Collision B is the most forceful, while Squirrel Collision C is the most gentle.